Four-dimensional Variational Assimilation for SO₂ Emission and its Application around the COVID-19 lockdown in the spring 2020 over China

Yiwen Hu[1,2], Zengliang Zang[2], Xiaoyan Ma[1], Yi Li[2], Yanfei Liang[3], Wei You[2], Xiaobin Pan[2], Zhijin Li[4]

[1]Collaborative Innovation Center on Forecast and Evaluation of Meteorological Disasters (CIC-FEMD), Key Laboratory for Aerosol-Cloud-Precipitation of China Meteorological Administration, Nanjing University of Information Science & Technology, Nanjing, 210044, China
[2]College of Meteorology and Oceanography, National University of Defense Technology, Changsha, 410073, China
[3]No. 32145 Unit of PLA, Xinxiang, 453000, China
[4]University of California Los Angeles, California, 91109, USA

Correspondence to: Zengliang Zang (zzlqxxy@163.com) and Xiaoyan Ma (xma@nuist.edu.cn)

Abstract. Emission inventories are essential for modeling studies and pollution control, but traditional emission inventories have large uncertainties and are often not real-time because they are highly human resource demanding to develop. In this study, a four-dimensional variational assimilation (4DVAR) system was developed to optimize sulfur dioxide (SO₂) emissions by assimilating hourly SO₂ concentrations. An observation system simulation experiment was conducted to evaluate the performance of the system. This evaluation indicates that the 4DVAR system can effectively reduce the uncertainty in SO₂ emissions at a regional level. The 4DVAR system was then applied to optimize SO₂ emissions during the early period of COVID-19 (from January 17 to February 6, 2020), and the reduction in SO₂ emissions was assessed in comparison with the 2016 inventory. The hourly surface SO₂ observations were assimilated. The results show that the emissions in 2020 decreased by 18.0% compared with those in 2019, indicating a significant decrease between 2019 and 2020 due to the COVID-19 related lockdown. Three forecast experiments were conducted using emissions in 2016, 2019, and 2020 to demonstrate the effects of optimized emissions. The root mean square error in 2020 decreased by 47.9% and the correlation coefficient increased by 300.0% compared with 2016 emissions. This suggests that the 4DVAR system can effectively optimize emissions to describe the actual change in SO₂ emissions during special events and improve the forecast skill.

Key words: 4DVAR; Sulfur dioxide; Emission inventory; WRF-Chem

1 Introduction

Sulfur dioxide (SO₂) can cause acid rain through sulfuric acid formation, destroying buildings and harming aquatic and terrestrial ecosystems (Saikawa et al., 2017; Zheng et al., 2018). SO₂ is also a precursor of sulfate aerosols, which directly affects the radiation budget and causes haze pollution. Therefore, SO₂ emission significantly impacts the ecological

environment. SO_2 pathway in the atmosphere is generally investigated using chemistry transport models (CTMs) that estimate the three-dimensional changes in SO_2 concentrations. Thus, accurately estimating SO_2 emissions is important for understanding spatiotemporal distribution of SO_2 concentrations in CTMs (Zeng and Wu, 2021).

35   SO_2 emission is generally estimated using the "bottom-up" approach, which requires direct observation of all possible sources' activities and emission factors (Zhao et al., 2022). However, the estimates are subject to significant uncertainties because of limited available observations, with difference among existing inventories as high as 42% (Granier et al., 2011). Saikawa et al. (2017) compared five types of emission inventories and found a significant difference in SO_2 emissions from the power sector owing to the difference in the assumed timing of installation of flue gas desulfurization in coal-fired power plants. Moreover, most "bottom-up" emissions are recorded as annual or monthly amounts, which need to be

40   spatiotemporally allocated into gridded hourly emissions for regional air quality model applications and cause uncertainty in grid emissions (Peng et al., 2017; Peng et al., 2018; Zeng and Wu, 2018). Several control strategies, such as strengthening emission standards, phasing out obsolete industrial capacity, small but high-emitting factories, have been implemented in China (Zheng et al., 2018), which have markedly reduced the emissions. However, varying extents of control policies implemented in different regions, have led to large spatiotemporal changes in emission values (Chen et al., 2019a; Dai et al.,

45   2021). Such complex changes in SO_2 emission did not reflect in the "bottom-up" estimates. Differences in the spatiotemporal control also caused additional uncertainties in gridded hourly emissions reducing their accuracy (Zeng et al., 2020).

       In contrast to the "bottom-up" approach, data assimilation (DA) provides a "top-down" approach, where the ensemble Kalman filter (EnKF) and four-dimensional variational DA (4DVAR) are two of the most explored algorithms. The EnKF method uses flow-dependent covariance generated by an ensemble of model outputs to convert observational information

50   into emissions (Tang et al., 2013; Ma et al., 2019), and has been used to estimate both aerosols and gas-phase emissions, such as SO_2, NOx, CO, and particulate matter, to estimate total regional and global emissions. (Huneeus et al., 2012; Huneeus et al., 2013; Miyazaki et al., 2012; Miyazaki et al., 2014; Tang et al., 2013; Tang et al., 2016; Chu et al., 2018). For example, Peng et al. (2017, 2018) developed an EnKF system to include more spatiotemporal emission characteristics over China using hourly surface observations as constraints, and the forecasting results with optimized emissions are

55   more accurate than those with background emissions. SO_2 forecasts with optimized emissions were improved for the 72-h forecast range, which decreased the root-mean-square errors (RMSEs) 30% compared with those with background emission. Feng et al. (2019) quantitatively optimized gridded CO emissions in China using hourly surface CO measurements using the Weather Research and Forecasting (WRF)/CMAQ model and EnKF algorithm. Optimized CO emissions in December 2017 were found to be 17% lower than those in December 2013. Moreover, the accuracy analysis field of EnKF depends on the

60   difference between the ensemble members. However, this difference usually converges gradually, and the background emissions of different members become similar during DA cycling of the EnKF (Chen et al., 2019). The EnKF is less effective when the difference between ensemble members is insufficient because of the small ensemble spread (Dai et al., 2021).

A 4DVAR method can be used to estimate emissions based on the adjoint model of a CTM, which canbe described as
65 the inverse process of the forward CTM (Bao et al., 2019; Yumimoto and Uno, 2006; Yumimoto et al., 2007; Wang et al.,
2021). Several studies have shown that 4DVAR is a promising tool for deriving the emission rates (Dubovik et al., 2008;
Hakami et al., 2005; Müller and Stavrakou, 2005; Elbern et al., 2007; Yumimoto et al., 2007; Yumimoto et al., 2008). Müller
and Stavrakou (2005) and Stavrakou and Atmospheres (2006) estimated CO and NOx emissions based on a 4DVAR system
using satellite data as a constraint. They showed that the optimized CO emission was 2900 Tg yr^{-1}, which was ~5% higher
70 than the background emission. Henze et al. (2007) developed an adjoint model based on the GEOS-Chem model and used it
to optimize the SOx, NOx, and NH$_3$ emissions. The model was also used to investigate the sensitivity of modeled aerosol
concentrations to their precursor emissions, suggesting that the relationship between the two mainly depended on
thermodynamic competition. Wang et al. (2012) followed Henze et al. (2007) and applied their adjoint model to constrain
dust emissions by assimilated aerosol optical depth from Moderate Resolution Imaging Spectroradiometer. They showed that
75 the optimized emissions decreased by 51% compared with the a-prior emissions, with a total decrease in emissions from 9.36
Tg to 4.55 Tg. The emissions based on "top-down" approach can reduce the uncertainty of "bottom-up" emissions, and
provide a more accurate emission for a special event than traditional emissions.

Emergence of the coronavirus pandemic (COVID-19) between the end of 2019 and the beginning of 2020 (Wang et al.,
2020) impacted over 200 countries. To control the rapid spread of the virus and protect people's health, Wuhan was the first
80 city to restrict travel and impose social distancing measures on January 23, 2020, followed by the entire Hubei province a
day later (Wuhan city is in the Hubei Province). Subsequently, all provinces in China successively implemented a national
emergency response to major public health emergencies. Because of lockdown during the pandemic, human activities, such
as industrial production and transportation, decreased sharply, which significantly decreases pollutant emissions (Filonchyk
et al., 2020; Forster et al., 2020; Ghahremanloo et al., 2021; Keller et al., 2021; Li et al., 2020; Miyazaki et al., 2020; Li et al.,
85 2021; Huang et al., 2021a). Zhang et al. (2020), Li et al. (2020), and Huang et al. (2021b) estimated the NOx emissions over
China during this period and observed a decreasing trend owing to human activity reduction. This study analyzes the
changes in SO$_2$ emission sources with respect to the COVID-19 pandemic.

We developed a 4DVAR SO$_2$ emission system to optimize its emission inventories using the WRF model coupled with
chemistry (WRF-Chem). Factors, such as transport, dry/wet deposition, emission, vertical mixing, and SO$_2$ chemicals were
90 implemented to describe the pathway of SO$_2$ in WRF-Chem. The observing systems simulation experiment (OSSE) was first
conducted to evaluate the performance of the 4DVAR system, which was then applied to investigate the changes in SO$_2$
emission in China, especially Central China, during the COVID-19 lockdown, by assimilating hourly surface SO$_2$
observations.

The remainder of this paper is organized as follows. The methodology, including the WRF-Chem and 4DVAR system
95 configurations and their adjoint model, is described in Section 2. The observational data are also presented in this section. In
Section 3, details of the OSSE are provided to verify the performance of the 4DVAR system, and the spatiotemporal changes
in SO$_2$ emission during the COVID-19 lockdown are estimated. SO$_2$ simulations using optimized emissions were also

verified against observations to show the improvements in emission data. Finally, a discussion and conclusions are presented in section 4.

2 Method and Data

2.1 WRF-Chem model

WRF-Chem is a fully coupled online air quality model involving sophisticated and comprehensive physical and chemical processes such as transport, deposition, emission, chemical transformation, photolysis, and radiation. The WRF-Chem version 3.9.1 was used to simulate and predict air pollutants. The center of the WRF-Chem domain (Fig. 1) is at 101.5 °E, 37.5 °N, covering the entire country with a 27 km horizontal resolution (169×211 grids). Additionally, 40 vertical layers extended from the surface to 50 hPa, with a more satisfactory resolution near the surface. Meteorological initial and boundary conditions were provided by the 1° × 1° National Centers for Environmental Prediction Global Final Analysis data at a 6-hour frequency. Most of the WRF-Chem settings were the same as those in Hu et al. (2022) (Table 1), i.e., the WRF Lin microphysics scheme (Lin et al., 1983), Rapid Radiative Transfer Model longwave (Mlawer et al., 1997), Goddard shortwave radiation schemes (Chou, 1994), Yonsei University (YSU) boundary layer scheme (Hong et al., 2006), Noah land surface model (Chen et al., 2010), and Grell-3D cumulus parameterization. Aerosol and gas-phase chemistry schemes include the model for simulating aerosol interactions and chemistry (MOSAIC-4 bin) and carbon bond mechanism-Z (CBMZ), respectively (Zaveri and Peters, 1999; Zaveri et al., 2008). The heterogeneous SO_2 reaction was also added to WRF-Chem (Sha et al., 2019), and anthropogenic emissions from the Multi-Resolution Emission Inventory for China (MEIC) in 2016 were used as the background emission input (Fig. 1).
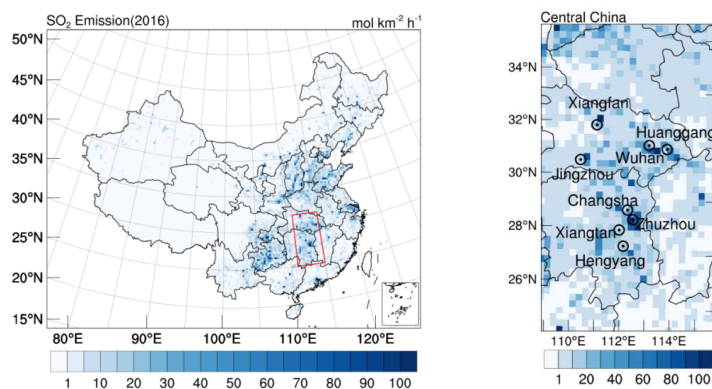
Figure 1: Spatial distribution of SO_2 emissions from MEIC for January 2016 and the study area. The red rectangle represents Central China. Black circle with dot is the location of large cities. Units: mol km^{-2} h^{-1}.

Table 1: WRF-Chem model configuration.

Physical or chemical process	Option
Microphysics	Lin microphysics scheme (Lin et al., 1983)
Longwave radiation	Rapid Radiative Transfer Model longwave (Mlawer et al., 1997)
Shortwave radiation	Goddard Space Flight Center shortwave radiation scheme (Chou, 1994)
Boundary layer scheme	Yonsei University (Hong et al., 2006)
Land surface model	Noah land surface model (Chen et al., 2010)
Cumulus parameterization	Grell 3-D scheme
Aerosol scheme	Model for Simulating Aerosol Interactions and Chemistry (MOSAIC-4 bin) (Zaveri et al., 2008)
Gas scheme	Carbon Bond Mechanism-Z (CBMZ) (Zaveri and Peters, 1999)

120

2.2 4DVAR system

4DVAR is a continuous data assimilation method that simultaneously assimilates a time series of observations over a time window. It produces an analysis that fit a set of observations taken over a time window, and evolution of the analyzed quantities is governed using a deterministic model as a strong constraint. The cost function of 4DVAR is as follows:

125
$$J = \frac{1}{2}(c_0 - c_0^b)^T B_c^{-1}(c_0 - c_0^b) + \frac{1}{2}\sum_{i=0}^{n-1}(e_i - e_i^b)^T B_{ei}^{-1}(e_i - e_i^b) + \frac{1}{2}\sum_{i=0}^{n}(y_i^o - H_i c_i)^T R_i^{-1}(y_i^o - H_i c_i) \tag{1}$$

where c_0 is the state variable that denotes the initial concentration vector, and c_0^b is the background concentration at zero time. The first term in Eq. 1 is the background term for the initial concentration field. e_i is the state variable that denotes the modified emission and e_i^b is the background emission. Subscripts of the variables represent the time window. The second term is the background term for emissions during the time window. B_c and B_{ei} are the background error covariances (BEC)

130 for the concentrations and emissions, respectively. The third term is the observation term, where y_i^o is the observation vector, H_i is the observation operator that computes the modeled observation estimate from the state variables and R_i is the error covariance matrix. c_i is the concentration at time i, which is subject to:

$$c_i = f_{i,i-1}(c_{i-1}, e_{i-1}) \tag{2}$$

The increment field of the initial SO₂ concentration can be written as $\delta c_0 = c_0 - c_0^b$, and the increment field of SO₂

135 emission as $\delta e_i = e_i - e_i^b$. The innovation vector is denoted as $d_i \equiv y_i^o - H_i(c_i)$, which is the difference between the observations and the model equivalent state. Thus, the cost function (1) can be written in an incremental form as follows:

$$J = \frac{1}{2}(\delta c_0)^T B_c^{-1}(\delta c_0) + \frac{1}{2}\sum_{i=0}^{n-1}(\delta e_i)^T B_{ei}^{-1}(\delta e_i) + \frac{1}{2}\sum_{i=0}^{n}(d_i - H_i \delta c_i)^T R_i^{-1}(d_i - H_i \delta c_i) \tag{3}$$

Using a linearization approximation, Eq. 2 becomes

$$\delta c_i = L_{i,i-1}\delta c_{i-1} + L_{i,i-1}\Gamma_{i-1}\delta e_{i-1} \tag{4}$$

140   where $L_{i,i-1}$ and Γ_{i-1} are Jacobians, and $i = 1,2,\cdots n$. Thus, a time integration can give Eq. 4 in the form:

$$\delta c_i = L_{i,0}\delta c_0 + \sum_{l=0}^{i-1} L_{i,l}\Gamma_l\delta e_l \tag{5}$$

where $L_{i,0}$ denotes the tangent linear model operator of the CTM acting on δc_0, and the subscript is the time step from i

to the initial time. $L_{i,l}\Gamma_l$ ($l = 0,1,\cdots i-1$) is the operator acting on δe_l and Γ_l is the emission term that converts emission to

concentration.

145   Available numerical algorithms can minimize the cost function in Eq. 3 (Courtier et al., 1994; Li and Navon, 2001). For

algorithms that can solve for large dimensions, the cost function gradient is required. This can be written with respect to δc_0

and δe_i ($i = 0,1,\cdots,n-1$) as:

$$\frac{\partial J}{\partial \delta c_0} = B_c^{-1}(\delta c_0) + \sum_{l=0}^{n} L_{l,0}^T H_l^T R_l^{-1}(d_l - H_l\delta c_l) \tag{6}$$

$$\frac{\partial J}{\partial \delta e_i} = B_{e_i}^{-1}(\delta e_i) + \sum_{l=i+1}^{n} \Gamma_i^T L_{l,i}^T H_l^T R_l^{-1}(d_l - H_l\delta c_l) \quad (i = 0,1,\cdots,n-1) \tag{7}$$

150   Note that, when $l = 0$ in Eq. 6, the $L_{0,0} = 1$. The window length is typically approximately six hours in operational

synoptic-scale numerical weather prediction centers. Additionally SO_2 lifetime is usually<6 h in a model grid (Fioletov et al.,

2015). Thus, we use a 6-h window ($n = 6$) for the 4DVAR system.

2.3 Adjoint model of 4DVAR system based on WRF-Chem

    The CTM in this study was based on WRF-Chem, which is a fully coupled online air quality model with sophisticated

155 and comprehensive physical and chemical processes. The governing equation for the concentration of species in WRF-Chem

can be written as:

$$\frac{\partial c}{\partial t} = -u\frac{\partial c}{\partial x} - v\frac{\partial c}{\partial y} - w\frac{\partial c}{\partial z} + \frac{\partial}{\partial x}\left(K_x\frac{\partial c}{\partial x}\right) + \frac{\partial}{\partial y}\left(K_y\frac{\partial c}{\partial y}\right) + \frac{\partial}{\partial z}\left(K_z\frac{\partial c}{\partial z}\right) - \frac{\partial c}{\partial t} \times e^{-\Lambda} - r \times \frac{\partial c}{\partial t} + V_m \times \frac{\rho_{air}}{\rho} \times \frac{\Delta S}{dz} \times E \tag{8}$$

where c is the gas/aerosol concentration, ∂x and ∂y are the horizontal resolutions of the model, ∂z is the vertical

resolution, and $u, v, and\ w$ denote the wind in $x, y, and\ z$ directions. Thus, the $u\frac{\partial c}{\partial x} + v\frac{\partial c}{\partial y} + w\frac{\partial c}{\partial z}$ is a transport term.

160 $K_x, K_y and\ K_z$ are turbulent exchange coefficient in $x, y, and\ z$ directions based on K theory of turbulence, and $\frac{\partial}{\partial x}\left(K_x\frac{\partial c}{\partial x}\right) +$

$\frac{\partial}{\partial y}\left(K_y\frac{\partial c}{\partial y}\right) + \frac{\partial}{\partial z}(K_z\frac{\partial c}{\partial z})$ is the turbulent term. For the large horizontal resolution study, the $\frac{\partial}{\partial x}(K_x\frac{\partial c}{\partial x}) \pm \frac{\partial}{\partial y}\left(K_y\frac{\partial c}{\partial y}\right)$ can be

neglect. $\frac{\partial c}{\partial t} \times e^{-\Lambda}$ denotes the wet deposition term, where Λ is the loss rate (Grell and Dévényi, 2002) and e is the base of

natural logarithms equal to 0.272, $r \times \frac{\partial c}{\partial t}$ is the chemical term, where r is the chemical reaction rate of the species, and

$V_m \times \frac{\rho_{air}}{\rho} \times \frac{\Delta S}{dz} \times E$ is the emission term, where E denotes the emission source of the species. $V_m = 22.4 \times 10^{-3}$ m³ mol⁻¹ is

165 the molar volume of the gas, ρ is the air density of the actual atmosphere (kg m⁻³), ρ_{air} is the standard air density indicating

the molar volume, and ΔS is the grid area.

In Eq. 4, L is the linearization approximation of the model. According to Eq. 8, L should include transport, dry/wet deposition, and chemical transformation, which can be written as L_{trans} L_{dry}, L_{wet}, and L_{chem}, respectively, using a linearization approximation (Jacob, 2000; Sha et al., 2019), where Γ is the emission term.

170 $\quad L_{trans} = -\bar{u}\frac{\partial c}{\partial x} - \bar{v}\frac{\partial c}{\partial y} - \bar{w}\frac{\partial c}{\partial z}$

(9)

$L_{trub} = \frac{\partial}{\partial z}(K_z \frac{\partial c}{\partial z})$

(10)

$L_{wet} = -\frac{\partial c}{\partial t} \times e^{-\bar{\Lambda}}$

175 (11)

$L_{chem} = -\bar{r} \times \frac{\partial c}{\partial t}$

(12)

$\Gamma = -V_m \times \frac{\rho_{air}}{\rho} \times \frac{\Delta S}{dz} \times E$

(13)

180 $\quad$ The variables in Eqs. 9–12 with superscript "−" denote the average values during a time step. Thus, the linearization Eq. 8 can be written as:

$\frac{\partial c}{\partial t} = L + \Gamma = L_{trans} + L_{trub} + L_{wet} + L_{chem} + \Gamma$ $\hspace{4cm}$ (14)

In addition, the vertical turbulence term (L_{trub}) for the surface level is $\frac{\partial c}{\partial z} \times v_d$, which denotes the dry deposition term, and v_d is the dry deposition velocity.

185

2.4 Observational and background error covariances

R_i in Eq. 1 is the observational error covariance for a set of observations (y_i), where B_c and B_{e_i} are the BECs for the concentrations and emissions, respectively. In a DA system, R_i and BEC play important roles in successful assimilation. R_i is derived from the measurement error (observed value error) and representative error (error of observation operator H),

190 which affect the weight of the observed data in assimilation. The observation error is defined as follows:

$\varepsilon_{SO_2} = \sqrt{\varepsilon_r{}^2 + \varepsilon_o{}^2}$ $\hspace{6cm}$ (15)

where ε_{SO_2} is the observation error of the assimilation variable, which is the SO_2 concentration in this experiment, ε_o is the measurement error, and ε_r is the representative error.

BECs (B_c and B_{e_i} in Eq. 1) are the error covariance matrices of SO$_2$ concentrations and emissions. Practically, the BEC

195   is too large to be handled numerically. Thus, we followed the method used by Li et al. (2013) and Zang et al. (2016) to
simplify B:

$$B = DCD^T \tag{16}$$

where D is the RMSE matrix and C is the correlation matrix.

C can be simplified by the Cholesky factorization and Kronecker product method (Li et al., 2013) as:

200    $$C^{\frac{1}{2}} = C_x^{\frac{1}{2}} \otimes C_y^{\frac{1}{2}} \otimes C_z^{\frac{1}{2}} \tag{17}$$

For SO$_2$ concentrations, the BEC used one month of the 48 h and 24 h forecast differences were used as the background
error. These differences were generated from January 2020. For the state variables of emissions, D is diagonal with a 200%
error (Wang et al., 2012) and C is a lower triangular matrix with a diagonal matrix because the emission can be diffused by
advection and vertical mixing.

2.5 Observation and emission data

Hourly SO$_2$ data from the website of the China National Environmental Monitoring Center (http://www.cnemc.cn) were
used for assimilation and evaluation. A total of 1933 national control measurement sites existed in China in January 2020.
Most observational sites were located in central and eastern China, whereas the sites in the west were relatively sparse. Only
1425 stations were selected (randomly) for assimilation, while the data of the remaining 508 stations were used to verify the
210   improvement in using optimized emissions (Fig. 2). A strict criterion was used to remove SO$_2$ observations with values
exceeding 650 µg m^{-3} to ensure data quality (Chen et al., 2019).

The background emission data of anthropogenic emissions were obtained from the MEIC (http://www.meicmodel.org/)
developed by Tsinghua University, with a 0.25° × 0.25° resolution and 2016 as the base year. The MEIC is a "bottom-up"
emission inventory model covering 31 provinces in Chinese mainland, including eight major chemical species (Zhang et al.,
215   2009), and counts anthropogenic emissions from sources in five sectors (power, industry, residential, transportation, and
agriculture). Details of the technology-based approach and source classifications can be found in Zhang et al. (2009). The
actual emission inventory (0.25 °× 0.25 °) was preprocessed to match the model grid spacing (27 km).
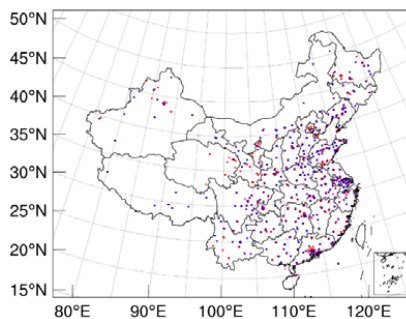
Figure 2: Locations of the 1425 SO₂ assimilation observation stations (red) and 508 independent observation stations (blue).

2.6 Experiment design

220   Figure 3 shows a flowchart of the optimization procedure of SO₂ emissions in a single time step from i to $i+n$. The background field of SO₂ concentrations was initialized based on WRF-Chem and background emission, running 10 days before the starting time to spin up the chemistry fields. A 6-h forecast was then performed to produce the SO₂ background field using the WRF-Chem model and background emissions. The meteorological and chemical parameters were recorded every ten minutes and then input into the 4DVAR emission assimilation system as a parameter. The tangent linear model

225   operator L calculated the physical and chemical processes in the adjoint model. The hourly SO₂ output was applied as a background field to calculate the innovation (d_i). Finally, by assimilating the hourly SO₂ observations, the 4DVAR system performed to obtain SO₂ optimized emissions and initial concentrations.

An OSSE was designed to evaluate the effect of the 4DVAR system. First, pseudo-observations were generated from a model using an emission inventory that was assumed as the "real" emission. A second inventory with a normally distributed emission was considered as the background emission, based on which an experiment was performed to obtain an optimized

230   emission by assimilating pseudo-observations using the 4DVAR system. Finally, the "real", background, and optimized emissions were compared to verify the effect of the 4DVAR system. The details of the experiment are described in Section 3.1.
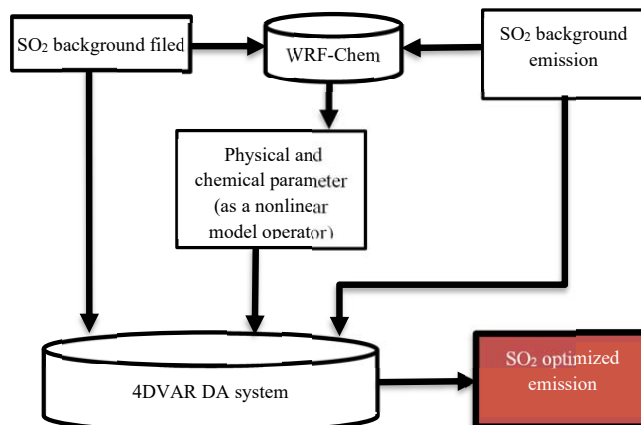
Figure 3: Flow chart of the procedure to optimize SO₂ emission in a single time step from i to $n + i$. The dark red box is the SO₂ optimized emission of output. Obs: observation.

In addition to the OSSE, three sets of experiments were performed on the emissions during COVID-19 (Table 3), including the Ctrl_2016, DA_2019, and DA_2020, to estimate the improvement of SO₂ forecasts using optimized emissions. National lockdown was imposed in Wuhan and other cities of Hubei on January 23 and 24, 2020, respectively. The national lockdown policies were implemented from January 26, 2020. Thus, we selected the week before the lockdown in Wuhan(January 17 to 23, 2020) and two weeks during the lockdown period (January 24 to February 6, 2020) as the study period. The optimized emissions for 2019 and 2020 were obtained from the 4DVAR system by assimilating the 2019 and 2020 surface SO₂ observations. Three experiments were run daily with 24 h forecasts from January 17 to 7 February 2020. All experiments used the same WRF-Chem domain settings and physicochemical parameters. The MEIC_2016 emissions were used in the Ctrl_2016 experiment. For the DA_2019 experiment, the 2019 optimized emissions were used to simulate SO₂ concentrations during the study period. For the DA_2020 experiment, the 2020 optimized emissions were applied. The SO₂ initial condition at 0000 UTC on January 17 was based on the spin-up forecasts at 0000 UTC on January 7, 2020 for all three forecast experiments. The SO₂ ICs were later obtained from the forecasting of the previous day for the three experiments.

Table 3: Details of the experiments designed in this study.

name	Emission	Forecast duration	Study period
Ctrl_2016	MEIC_2016	24 h	17 January - 7 February, 2020
DA_2019	The 2019 optimized	24 h	17 January - 7 February, 2020

| DA_2020 | The 2020 optimized | 24 h | 17 January - 7 February, 2020 |

3 Results

3.1 Observing Systems Simulation Experiment (OSSE)

255   An OSSE was conducted to verify the performance of the 4DVAR DA system. The "real" emissions included 273 sources (Fig. 4a). These emissions were evenly distributed, with 13 arrays and 9 columns. The "real" emission values (EM_real) at each grid were random. The hourly factors of EM_real were equal. The WRF-Chem model and EM_real emission were applied to simulate (because the assimilation window was 6 h) SO_2 concentrations for 30 h. SO_2 concentrations simulated by WRF-Chem were set as the "real" observation. The background emission (EM_back) included

260   273 sources having the same spatial distribution as EM_real (Fig. 4b). The value of EM_back were random with a mean value of 50 mol km^{-2} h^{-1}, and the hourly factors were equal between 24 hours. Both EM_real and EM_back were normally distributed, but did not correlate with each other.
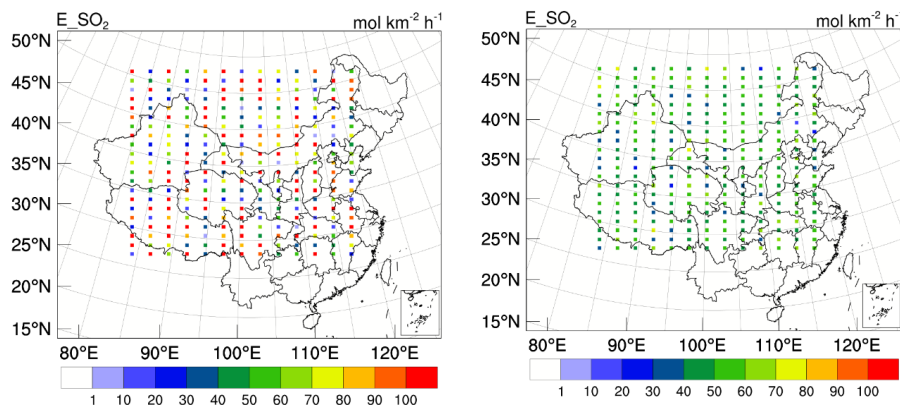
Figure 4: (a) Real emissions (EM_real) and (b) background emission (EM_back) of OSSE. Units are mol km^{-2} h^{-1}.

OSSE was performed using EM_back. The optimized emission (EM_new) was obtained from the 4DVAR emission

265   system by assimilating the hourly "real" SO_2 concentrations. Figure 5a shows a comparison of the 24 h average of EM_real emissions, EM_back and EM_new emissions. It was observed that the 4DVAR emission assimilation system can effectively improve emission accuracy. Compared with EM_back, the average bias of EM_new increased considerably (90%) from -18.7 to -1.9 mol km^{-2} h^{-1}. This suggests that the 4DVAR system can effectively correct system deviation of the emissions when the EM_back is underestimated or overestimated. The RMSE decreased from 43.3 to 16.8 mol km^{-2} h^{-1}, and the

270   correlation coefficient (CORR) increased from 0.01 to 0.90. This indicates that the 4DVAR assimilation system could

improve SO$_2$ emission estimation by assimilating the surface SO$_2$ concentrations. Even with large differences between the background and real values, the 4DVAR assimilation system can effectively reduce the deviation.

Figure 5b shows the size of the cost function for each inner iteration. In this example, the maximum number of iterations was ten considering the balance between calculation time and result accuracy. It shows that the cost function quickly converges with an increase in the number of iterations. After seven iterations, the cost function was stable and close to minimum. The J_b of the end iteration was 6.3% of the first iteration.
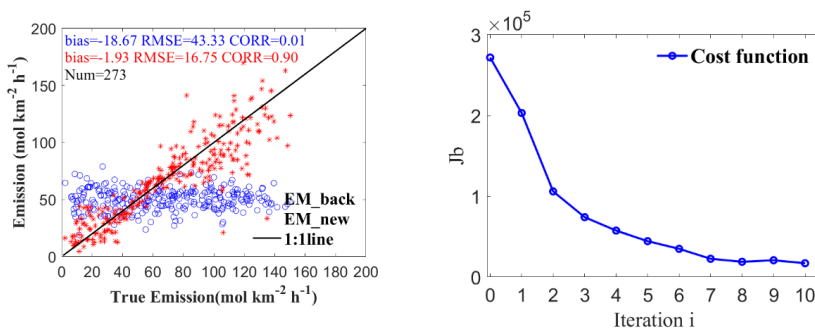
Figure 5: (a) Scatter plot between EM_real and EM_back/EM_new. (b) Cost function for each inner iteration. Units are mol km^{-2} h^{-1} for (a)

3.2 Emission changes

3.2.1 Temporal changes in emission

Figure 6 shows the hourly SO$_2$ concentrations and daily optimized SO$_2$ emissions for the Chinese mainland and Central China. The SO$_2$ emission trends were similar to those of SO$_2$ concentrations during the study period in both 2019 and 2020. In 2019, the lowest emissions occurred on February 3, 2019, followed which day is celebrated as Spring Festival in China that is the most important festival of the country. Increased SO$_2$ emissions during February 4–6, 2019, was mainly attributed to traditional firework displays during the Spring Festival (Wang et al., 2007; Zhang et al., 2020; Huang et al., 2021a). In 2020, complex changes were observed in SO$_2$ emission trends because of negligible human activities during COVID-19. The first peak in the country was 40.1 kg d^{-1} on January 24, 2020, because of the firework displays (Figs. 6a and 6b), after which the SO$_2$ emissions decreased because of national lockdown, when most factories shutting down and people staying at home to protect against coronavirus. SO$_2$ emissions in Central China peaked at 3.5 kg d^{-1} on January 24, 2020, due to firework displays, and a significant reduction began from January 26, 2020, because of national lockdown. Increased SO$_2$ concentrations on January 31, 2020, were mainly due to meteorological conditions, when there was no significant change in emissions.

295

(a) SO$_2$ concentration in China   (b) SO$_2$ emission in China

(c) SO$_2$ concentration in Central China   (d) SO$_2$ emission in Central China
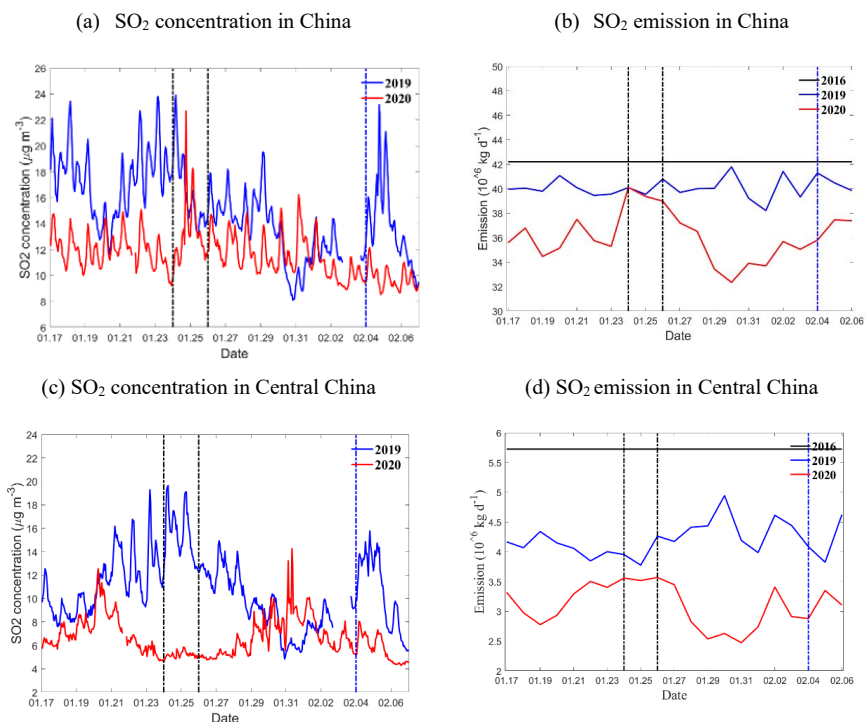
300 **Figure 6: Time series of hourly SO$_2$ concentration in (a) China and (c) Central China. Time series of daily SO$_2$ emission in (b) China and (d) Central China. Units are μg km^{-3} for (a) and (c), and 10^6 kg d^{-1} for (b) and (d). The Chinese Spring Festivals were on February 4 2019 and January 24 2020, respectively; January 26 2020 was the date of implementation of national lockdown.**

3.2.2 Spatial changes in emission

Figure 7 shows the spatial differences and variations in emission ratios in 2019 and 2020. Compared with the 2019
305 optimized emissions (Fig. 7a), the 2020 optimized emissions (Fig. 7b) decreased in most of the country due to the lockdown. The decrease in emissions (Fig. 7c) in most areas was <10 mol km^{-2} h^{-1}, but the ratios (Fig. 7d) were more significant than

20%. Zheng et al. (2020) showed that SO_2 emissions in China decreased by 29% in February 2020 compared to that in 2019. Nationwide emission reduction occurred because of the implementation national lockdown policies. The areas with increased SO_2 emissions were Northeast China, the Tibetan Plateau, Yunnan Province, and southeast coastal areas, where the

310   epidemic was less severe than in other areas (Kraemer Moritz et al., 2020; Tian et al., 2020). Most of the increase in SO_2 was <10 mol km^{-2} h^{-1}, but the positive rates were >100%, suggesting that new emission sources were generated. It is believed that these newly generated emissions were caused by relocating power plants and factories from cities to the surrounding villages.
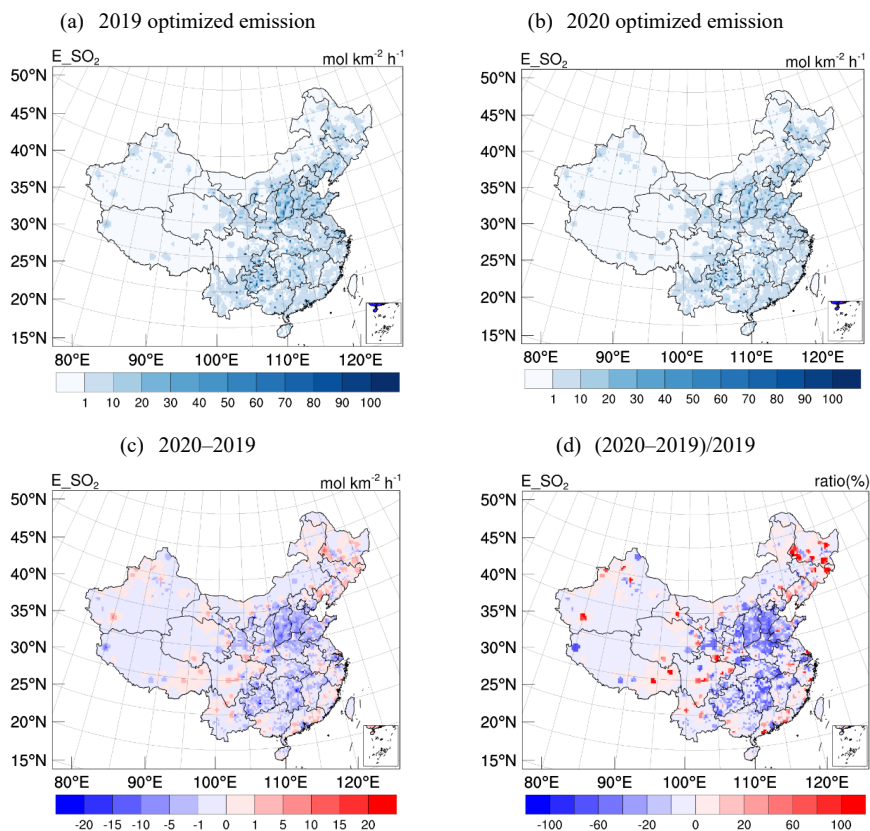
Figure 7: Optimized emissions in China for (a) 2019 and (b) 2020. (c) Differences between 2019 and 2020 optimized emissions and (d) ratios of (2020–2019)/2019. (Units are mol km^{-2} h^{-1} for (a), (b), and (c).)

315   Figure 8 shows the same observations as Fig. 7, but for central China. Hubei province was the first to implement a first-level response to major public health emergencies. The emissions in Wuhan were relatively lower than those in surrounding grid points because most of the factories were relocated to the countryside owing to China's recent emission reduction

policies (Figs. 8a and 8b) (Zheng et al., 2018; Bian et al., 2019; van der A et al., 2017). The highest emission value around Wuhan in 2019 was 475 mol km^{-2} h^{-1} and 203 mol km^{-2} h^{-1} in 2020, showing a reduction of 57%. Almost all emissions in the Hubei Province decreased slightly by 5–10 mol km^{-2} h^{-1} (Fig. 8c). The reduction percentage in these regions was over -40% (Fig. 8d). Remarkably, emission reduction occurred because most industries in central China closed during the epidemic. Slightly increased emissions were observed at some scatter points (<5 mol km^{-2} h^{-1}), possibly because of increased residential emissions due to home isolation.
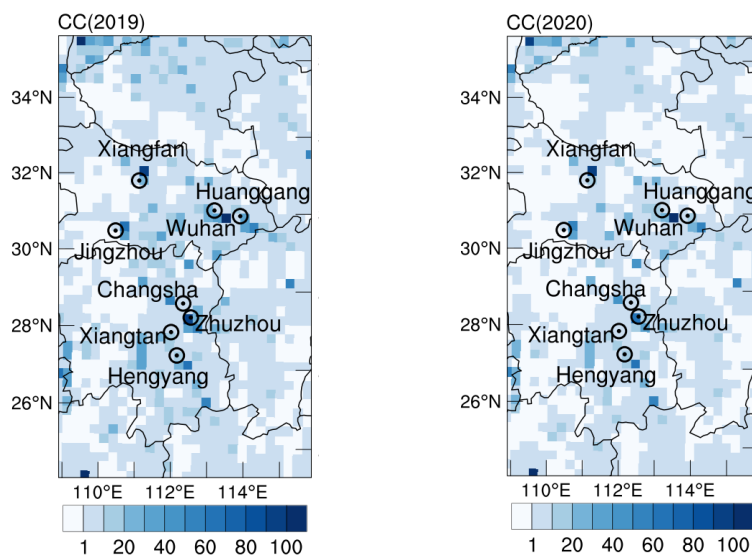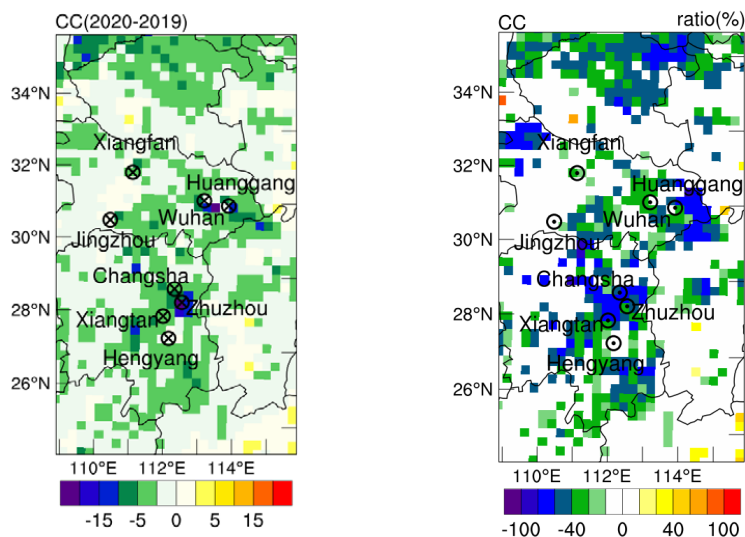
Figure 8: Parameters same as Figure 7, but for central China. (Units are mol km⁻² h⁻¹ for (a), (b) and (c). CC: central China)

3.2.3 Hourly emission

Figure 9 shows the average hourly emissions for 2016, 2019, and 2020 for the entire study period. The hourly factors for MEIC_2016 were obtained from the power plant report, with two peaks during the day at 0100 UTC (0900 BJ time – Beijing time) and 0900 UTC (1700 BJ time) to reflect the emissions during rush hours (Chen et al., 2019b; Hu et al., 2022). The emissions in 2019 and 2020 were lower than those of MEIC_2016 during 0600–1200 UTC (Fig. 9a). The main reason for this is the recent implementation of China's emission reduction policies. Studies have shown that the second peak (0900 UTC) of SO_2 emissions had weakened (Chen et al., 2019), which was also reflected in our hourly emission analysis. However, the 2019 and 2020 emissions were slightly higher than those of MEIC_2016 during 1600–2000 UTC. Consequently, the difference in the hourly factor between the optimized emissions and MEIC_2016 suggests changes in the hourly emission characteristics. Compared with the 2019 optimized emissions, the 2020 optimized emissions averagely decreased by -18.0%, reflecting reduction due to the lockdown during COVID-19.

The optimized emissions in 2019 and 2020 in Central China were significantly lower than the emissions in 2016 for each of the 24 h, with maximum reduction at 0900 UTC (Fig. 9b). Compared with 2019 optimized emissions, the 2020 emissions appreciably decreased by 22.3–42.1%. The first peak of the 2020 optimized emissions was delayed and occurred at 0200 UTC because of the national lockdown policies. The most significant reduction between 2019 and 2020 emissions was -120.4 × 10³ kg h⁻¹ at 01 UTC, reflecting the change in human activities at the first peak. Additionally, although the

decrease in SO_2 emission was moderate (-72.3×10^3 kg h^{-1}) at 1300 UTC, the reduction ratio (-54.5%) was the largest during 24 h.
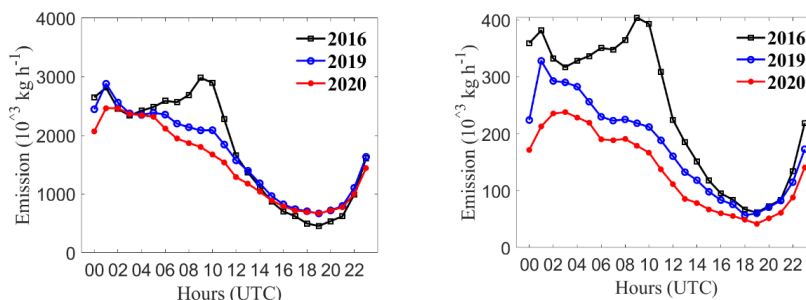
Figure 9: Hourly emission source for (a) China and (b) Central China (Unit: 10^3 kg h^{-1}).

3.3 Forecast improvement

Figure 10 shows the average 24-hour forecast of SO_2 concentrations in China for 2020 during the study period using MEIC_2016, 2019 and 2020 optimized emissions. It was observed that the DA_2020 experiment with the 2020 optimized emissions performed much better than the Ctrl_2016 and DA_2019 experiments, indicating that emission values are one of the most important factors for 24 h forecasts. The SO_2 concentrations in Ctrl_2016 and DA_2019 were significantly overestimated, especially during 0800–1800 UTC (Fig. 10a). Additionally, the 2020 optimized emission during 1800–2200 UTC were higher than MEIC_2016, but the SO_2 forecast concentrations with them were lower than those with MEIC_2016. This is possibly because the high values of the 2020 emissions were mainly located in the western and northwestern regions (Fig. 7), where were fewer sites in the western and northwestern regions, meanwhile, there were more measurement sites where the 2020 emissions have low values. Thus, when the concentrations in Fig. 10 were interpolated to the measurement sites and averaged to derive the mean concentrations in DA_2020, so the results were lower than those in Ctrl_2016. Compared to the Ctrl_2016 experiment, the RMSE of the DA_2020 experiment performed better during the study period, and the average RMSE decreased from 21.7 to 11.3 µg m^{-3}. For DA_2019, the RMSE was better than that for Ctrl_2016 over 24 h. The average CORR for the Ctrl_2016, DA_2019, and DA_2020 experiments were 0.2, 0.4, and 0.6, respectively. The average Bias of Ctrl_2016, DA_2019, and DA_2020 experiments were 5.9, 4.9, and -0.1 µg m^{-3}, respectively, suggesting that the 4DVAR method reduces the uncertainty of the background emissions.
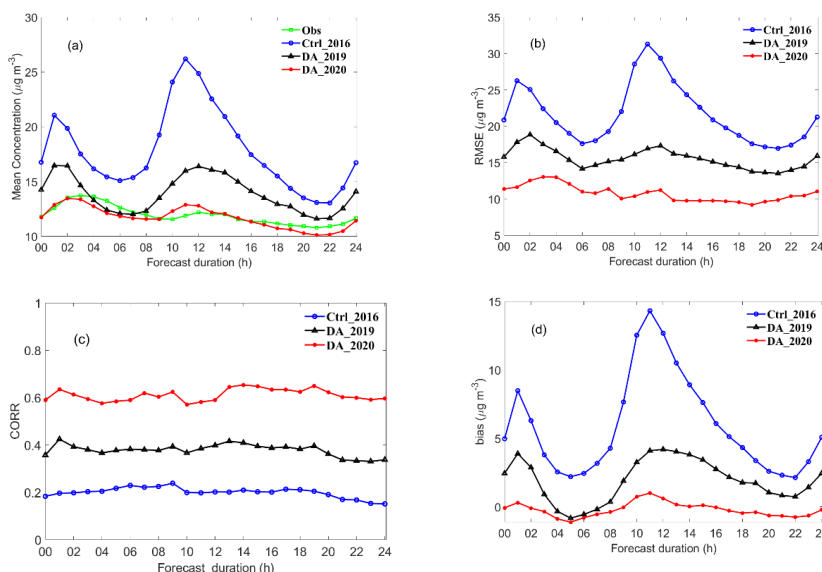
Figure 10: Forecast skill of SO₂ concentrations in China for the Ctrl_2016, DA_2019, and DA_2020 experiments during the study period in 2020: (a) Mean concentration, (b) RMSE, (c) CORR, and (d) bias. Unit is μg m⁻³ for (a), (b), and (d). Obs: Observation.

Figure 11 shows the same observations as Fig. 10, but for Central China. It also showed that the forecast skills of the DA_2019 and DA_2020 experiments were higher than those of Ctrl_2016. The average observation was <10 μg m⁻³, which is significantly lower than that for Chinese mainland (Fig. 10a). The Ctrl_2016 and DA_2019 experiments overestimated the SO₂ concentration in Central China, reflecting overestimation of MEIC_2016 and 2019 optimized emissions, which is consistent with the emission source (Fig. 8b). SO₂ forecast in the DA_2020 experiment was closest to the observations, with values <10 μg m⁻³. Compared to Ctrl_2016, the average bias of DA_2020 experiment decreased from 20.1 to 3.5 μg m⁻³, the average RMSE decreased from 30.0 to 7.4 μg m⁻³, and the average CORR increased from 0.2 to 0.5, compared with the Ctrl_2016 experiment (Figs. 11b to 11d). Notably, the bias of the DA_2020 experiment was positive (Fig. 11d), and the average concentration was higher than the observations (Fig. 11a), suggesting an overestimation of the 2020 optimized emissions. This may be because the actual emissions in Central China decreased significantly, and the analyzed field (optimized emissions) is a balance between the background field (background emissions) and observations. Thus, the optimized emissions are still affected by the background field.
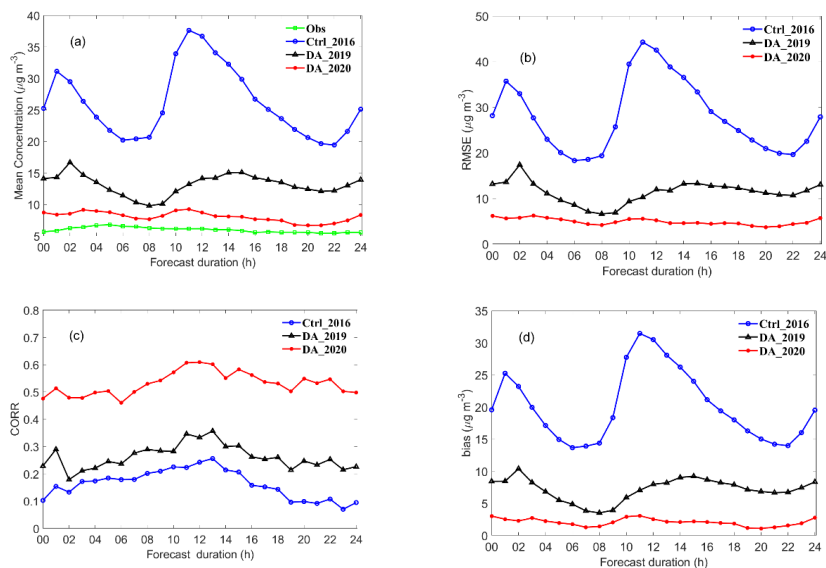
375   **Figure 11: Parameters same as Fig. 10, but for Central China.**

4 Conclusions

In this study, we developed a 4DVAR system based on the WRF-Chem model, where the initial SO_2 concentration and emissions were set as the state variables to estimate SO_2 emissions. An adjoint model was developed focusing on the processes of transport, dry/wet deposition, and SO_2 chemical reactions derived from the WRF-Chem model. Observations of

380   the hourly SO_2 concentration were assimilated to optimize SO_2 emissions, which were used to improve the SO_2 forecasting skill.

OSSE was performed to evaluate the performance of the 4DVAR system. The newly improved emission (EM_new) was obtained by assimilating the pseudo-observations, and EM_back was set as the background emission. Compared with EM_back, the average bias of EM_new decreased from -18.7 to -1.9 mol km^{-2} h^{-1}. The average RMSE decreased from 43.3

385   to 16.8 mol km^{-2} h^{-1}, and the average CORR increased from 0.01 to 0.9. These results suggest that the developed 4DVAR system can effectively improve estimation accuracy of the emission source by assimilating the surface SO_2 concentration.

The 4DVAR system was then applied to investigate SO_2 emission changes during the COVID-19 lockdown in China, with special focus on Central China. The MEIC_2016 emissions were set as the background value, and the observational data were assimilated to optimize SO_2 emissions from January 17 to February 6 in 2019 and 2020. The results showed a

390   significant reduction in emissions, with 2019 and 2020 optimized emissions decreasing by 5.0% and 14.5%, respectively.

The 2020 optimized emissions dropped by more than 20 % in most parts of Central China compared to the 2019 optimized emissions, owing to reduction in human activity during COVID-19. The largest decrease in emissions was around Wuhan, which COVID-19 heavily hit by the time, with a decline of 57%. Hourly average emissions were analyzed to estimate the changes between 2019 and 2020. Compared with 2019 optimized emissions, the 2020 optimized emissions decreased on an

395 average by 18.0%, reflecting the reduction of SO_2 emissions due to the lockdown. For Central China, the 2020 optimized emissions decreased by 22.3–42.1% compared with the 2019 optimized emissions.

Three sets of forecast experiments for 2020, using MEIC_2016, 2019, and 2020 emissions, were conducted to illustrate the effects of the optimized emissions. The experiment with MEIC_2016 emissions overestimated the SO_2 concentration forecast, whereas the experiment with 2019 optimized emissions decreased the concentrations but still overestimated the

400 values. The forecast skill of the experiment with the 2020 emissions was the best, where the RMSE decreased from 21.7 to 11.3 $\mu g\ m^{-3}$, and the CORR increased from 0.2 to 0.6 compared to the 2016 emission. For Central China, the average bias and RMSE in the DA_2020 experiment decreased by 87.7% and 77.0%, respectively, and the average CORR increased by 201.3%.

However, the conducted study has some limitations. Only hourly surface SO_2 observations were used to constrain the

405 emission sources. The spatial distribution of surface observation sites was uneven, and there were fewer sites in the northwest and southwest regions, resulting in limited adjustments to emission sources in these regions. In future, satellite data will be used to adjust the emission source to address the lack of surface observation data. Furthermore, simultaneous optimization of SO_2 concentrations and emissions will be implemented in a 4DVAR system, and multi-source observation data will be used to improve its performance.

410

Author contributions: Zengliang Zang designed the overall research; Yiwen Hu performed experiments; Yanfei Liang, Wei You and Xiaobin Pan contributed to the development of the DA system; Zengliang Zang and Xiaoyan Ma provided funds; Yiwen Hu, Zengliang Zang, and Xiaoyan Ma. wrote the paper, with contributions from all co-authors; Xiaoyan Ma, Zengliang Zang and Zhijin Li developed the

415 mathematical formulation and reviewed the paper. All authors have read and agreed to the published version of the manuscript.

Funding: This research was funded by the National Natural Science Foundation of China (Grant Nos. 41775123, 42061134009, 41975167, and 41975002). This research was supported by the National Key Scientific and Technological Infrastructure project "Earth System Science Numerical Simulator Facility" (EarthLab).

Data availability: The data and data analysis method are available upon request.

420 **Competing interests:** The authors declare that they have no conflict of interest.

Acknowledgments: NCEP FNL reanalysis data were downloaded from https://rda.ucar.edu/datasets/ds083.2/, last access: 13 April 2022. The MEIC 2016 emission sources were developed by Tsinghua University (http://meicmodel.org/?lang=en, last access: 13 April 2022). The hourly SO_2 observations were downloaded from the CNEMC website (http://www.cnemc.cn, last access: 13 April 2022).

425 **References**

Bao, Y., Zhu, L., Guan, Q., Guan, Y., Lu, Q., Petropoulos, G. P., Che, H., Ali, G., Dong, Y., Tang, Z., Gu, Y., Tang, W., and Hou, Y.: Assessing the impact of Chinese FY-3/MERSI AOD data assimilation on air quality forecasts: Sand dust events in northeast China, Atmospheric Environment, 205, 78-89, 10.1016/j.atmosenv.2019.02.026, 2019.

Chen, D., Liu, Z., Ban, J., and Chen, M.: The 2015 and 2016 wintertime air pollution in China: SO2 emission changes
430 derived from a WRF-Chem/EnKF coupled data assimilation system, Atmospheric Chemistry and Physics, 19, 8619-8650, 10.5194/acp-19-8619-2019, 2019a.

Chen, D., Liu, Z., Ban, J., and Chen, M.: The 2015 and 2016 wintertime air pollution in China: SO2 emission changes derived from a WRF-Chem/EnKF coupled data assimilation system, Atmos. Chem. Phys., 19, 8619-8650, 10.5194/acp-19-8619-2019, 2019b.

435 Chen, Y., Yang, K., Zhou, D., Qin, J., and Guo, X.: Improving the Noah Land Surface Model in Arid Regions with an Appropriate Parameterization of the Thermal Roughness Length, Journal of Hydrometeorology, 11, 995-1006, 10.1175/2010JHM1185.1, 2010.

Chou, M.: An efficient thermal infrared radiation parameterization for use in general circulation models, 1994.

Chu, K., Peng, Z., Liu, Z., Lei, L., Kou, X., Zhang, Y., Bo, X., and Tian, J.: Evaluating the Impact of Emissions Regulations
440 on the Emissions Reduction During the 2015 China Victory Day Parade With an Ensemble Square Root Filter, Journal of Geophysical Research: Atmospheres, 123, 4122-4134, https://doi.org/10.1002/2017JD027631, 2018.

Courtier, P., Thépaut, J. N., and Hollingsworth, A.: A strategy for operational implementation of 4D-Var, using an incremental approach, Quarterly Journal of the Royal Meteorological Society, 120, 1367-1387, https://doi.org/10.1002/qj.49712051912, 1994.

445 Dai, T., Cheng, Y., Goto, D., Li, Y., Tang, X., Shi, G., and Nakajima, T.: Revealing the sulfur dioxide emission reductions in China by assimilating surface observations in WRF-Chem, Atmos. Chem. Phys., 21, 4357-4379, 10.5194/acp-21-4357-2021, 2021.

Dubovik, O., Lapyonok, T., Kaufman, Y. J., Chin, M., Ginoux, P., Kahn, R. A., and Sinyuk, A.: Retrieving global aerosol sources from satellites using inverse modeling, Atmos. Chem. Phys., 8, 209-250, 10.5194/acp-8-209-2008, 2008.

450 Elbern H., Strunk, A., Schmidt, H., and Talagrand, O.: Emission rate and chemical state estimation by 4-dimensional, Atmospheric Chemistry and Physics, 2007.

Filonchyk, M., Hurynovich, V., Yan, H., Gusev, A., and Shpilevskaya, N.: Impact Assessment of COVID-19 on Variations of SO2, NO2, CO and AOD over East China, Aerosol and Air Quality Research, 20, 1530-1540, 10.4209/aaqr.2020.05.0226, 2020.

455 Fioletov, V. E., McLinden, C. A., Krotkov, N., and Li, C.: Lifetimes and emissions of SO2 from point sources estimated from OMI, Geophysical Research Letters, 42, 1969-1976, https://doi.org/10.1002/2015GL063148, 2015.

Forster, P. M., Forster, H. I., Evans, M. J., Gidden, M. J., Jones, C. D., Keller, C. A., Lamboll, R. D., Quéré, C. L., Rogelj, J.,

Rosen, D., Schleussner, C.-F., Richardson, T. B., Smith, C. J., and Turnock, S. T.: Current and future global climate impacts resulting from COVID-19, Nature Climate Change, 10, 913-919, 10.1038/s41558-020-0883-0, 2020.

460 Ghahremanloo, M., Lops, Y., Choi, Y., and Mousavinezhad, S.: Impact of the COVID-19 outbreak on air pollution levels in East Asia, Sci Total Environ, 754, 142226, 10.1016/j.scitotenv.2020.142226, 2021.

Granier, C., Bessagnet, B., Bond, T., D'Angiola, A., Denier van der Gon, H., Frost, G. J., Heil, A., Kaiser, J. W., Kinne, S., Klimont, Z., Kloster, S., Lamarque, J.-F., Liousse, C., Masui, T., Meleux, F., Mieville, A., Ohara, T., Raut, J.-C., Riahi, K., Schultz, M. G., Smith, S. J., Thompson, A., van Aardenne, J., van der Werf, G. R., and van Vuuren, D. P.: Evolution of

465 anthropogenic and biomass burning emissions of air pollutants at global and regional scales during the 1980–2010 period, Climatic Change, 109, 163, 10.1007/s10584-011-0154-1, 2011.

Grell, G. A., and Dévényi, D.: A generalized approach to parameterizing convection combining ensemble and data assimilation techniques, 29, 38-31-38-34, https://doi.org/10.1029/2002GL015311, 2002.

Hakami, A., Henze, D. K., Seinfeld, J. H., Chai, T., Tang, Y., Carmichael, G. R., and Sandu, A.: Adjoint inverse modeling of

470 black carbon during the Asian Pacific Regional Aerosol Characterization Experiment, Journal of Geophysical Research: Atmospheres, 110, n/a-n/a, 10.1029/2004jd005671, 2005.

Henze, D. K., Hakami, A., and Seinfeld, J. H.: Development of the adjoint of GEOS-Chem, Atmos. Chem. Phys., 7, 2413-2433, 10.5194/acp-7-2413-2007, 2007.

Hong, S.-Y., Noh, Y., and Dudhia, J.: A New Vertical Diffusion Package with an Explicit Treatment of Entrainment

475 Processes, Monthly Weather Review, 134, 2318-2341, 10.1175/mwr3199.1, 2006.

Hu, Y., Zang, Z., Chen, D., Ma, X., Liang, Y., You, W., Pan, X., Wang, L., Wang, D., and Zhang, Z.: Optimization and Evaluation of SO2 Emissions Based on WRF-Chem and 3DVAR Data Assimilation, Remote Sensing, 14, 10.3390/rs14010220, 2022.

Huang, C., Wang, T., Niu, T., Li, M., Liu, H., and Ma, C.: Study on the variation of air pollutant concentration and its

480 formation mechanism during the COVID-19 period in Wuhan, Atmospheric Environment, 251, 118276, https://doi.org/10.1016/j.atmosenv.2021.118276, 2021a.

Huang, X., Ding, A., Gao, J., Zheng, B., Zhou, D., Qi, X., Tang, R., Wang, J., Ren, C., Nie, W., Chi, X., Xu, Z., Chen, L., Li, Y., Che, F., Pang, N., Wang, H., Tong, D., Qin, W., Cheng, W., Liu, W., Fu, Q., Liu, B., Chai, F., Davis, S. J., Zhang, Q., and He, K.: Enhanced secondary pollution offset reduction of primary emissions during COVID-19 lockdown in China, National

485 Science Review, 8, 10.1093/nsr/nwaa137, 2021b.

Huneeus, N., Chevallier, F., and Boucher, O.: Estimating aerosol emissions by assimilating observed aerosol optical depth in a global aerosol model, Atmospheric Chemistry and Physics, 12, 4585-4606, 10.5194/acp-12-4585-2012, 2012.

Huneeus, N., Boucher, O., and Chevallier, F.: Atmospheric inversion of SO2 and primary aerosol emissions for the year 2010, Atmospheric Chemistry and Physics, 13, 6555-6573, 10.5194/acp-13-6555-2013, 2013.

490 Jacob, D. J.: Heterogeneous chemistry and tropospheric ozone, Atmospheric Environment, 34, 2131-2159, https://doi.org/10.1016/S1352-2310(99)00462-8, 2000.

Keller, C. A., Evans, M. J., Knowland, K. E., Hasenkopf, C. A., Modekurty, S., Lucchesi, R. A., Oda, T., Franca, B. B., Mandarino, F. C., Díaz Suárez, M. V., Ryan, R. G., Fakes, L. H., and Pawson, S.: Global impact of COVID-19 restrictions on the surface concentrations of nitrogen dioxide and ozone, Atmospheric Chemistry and Physics, 21, 3555-3592, 10.5194/acp-21-3555-2021, 2021.

Kraemer Moritz, U. G., Yang, C.-H., Gutierrez, B., Wu, C.-H., Klein, B., Pigott David, M., null, n., du Plessis, L., Faria Nuno, R., Li, R., Hanage William, P., Brownstein John, S., Layan, M., Vespignani, A., Tian, H., Dye, C., Pybus Oliver, G., and Scarpino Samuel, V.: The effect of human mobility and control measures on the COVID-19 epidemic in China, Science, 368, 493-497, 10.1126/science.abb4218, 2020.

Li, L., Li, Q., Huang, L., Wang, Q., Zhu, A., Xu, J., Liu, Z., Li, H., Shi, L., Li, R., Azari, M., Wang, Y., Zhang, X., Liu, Z., Zhu, Y., Zhang, K., Xue, S., Ooi, M. C. G., Zhang, D., and Chan, A.: Air quality changes during the COVID-19 lockdown over the Yangtze River Delta Region: An insight into the impact of human activity pattern changes on air pollution variation, Sci Total Environ, 732, 139282, 10.1016/j.scitotenv.2020.139282, 2020.

Li, M., Wang, T., Xie, M., Li, S., Zhuang, B., Fu, Q., Zhao, M., Wu, H., Liu, J., Saikawa, E., and Liao, K.: Drivers for the poor air quality conditions in North China Plain during the COVID-19 outbreak, Atmospheric Environment, 246, 118103, https://doi.org/10.1016/j.atmosenv.2020.118103, 2021.

Li, Z., and Navon, I. M.: Optimality of variational data assimilation and its relationship with the Kalman filter and smoother, Quarterly Journal of the Royal Meteorological Society, 127, 661-683, https://doi.org/10.1002/qj.49712757220, 2001.

Li, Z., Zang, Z., Li, Q. B., Chao, Y., Chen, D., Ye, Z., Liu, Y., and Liou, K. N.: A three-dimensional variational data assimilation system for multiple aerosol species with WRF/Chem and an application to PM2.5; prediction, Atmospheric Chemistry and Physics, 13, 4265-4278, 10.5194/acp-13-4265-2013, 2013.

Lin, Y., Farley, R., and Orville, H. D. J. J. o. A. M.: Bulk Parameterization of the Snow Field in a Cloud Model, 22, 1065-1092, 1983.

Ma, C., Wang, T., Mizzi, A. P., Anderson, J. L., Zhuang, B., Xie, M., and Wu, R.: Multiconstituent Data Assimilation With WRF-Chem/DART: Potential for Adjusting Anthropogenic Emissions and Improving Air Quality Forecasts Over Eastern China, Journal of Geophysical Research: Atmospheres, 10.1029/2019jd030421, 2019.

Miyazaki, K., Eskes, H. J., and Sudo, K.: Global NOx emission estimates derived from an assimilation of OMI tropospheric NO2 columns, Atmospheric Chemistry and Physics, 12, 2263-2288, 10.5194/acp-12-2263-2012, 2012.

Miyazaki, K., Eskes, H. J., Sudo, K., and Zhang, C.: Global lightning NOx production estimated by an assimilation of multiple satellite data sets, Atmospheric Chemistry and Physics, 14, 3277-3305, 10.5194/acp-14-3277-2014, 2014.

Miyazaki, K., Bowman, K., Sekiya, T., Jiang, Z., Chen, X., Eskes, H., Ru, M., Zhang, Y., and Shindell, D.: Air Quality Response in China Linked to the 2019 Novel Coronavirus (COVID-19) Lockdown, Geophys Res Lett, 47, e2020GL089252, 10.1029/2020GL089252, 2020.

Mlawer, E. J., Taubman, S. J., Brown, P. D., Iacono, M. J., and Clough, S. A.: Radiative transfer for inhomogeneous atmospheres: RRTM, a validated correlated-k model for the longwave, 102, 16663-16682,

https://doi.org/10.1029/97JD00237, 1997.

Müller, J. F., and Stavrakou, T.: Inversion of CO and NOx emissions using the adjoint of the IMAGES model, Atmos. Chem. Phys., 5, 1157-1186, 10.5194/acp-5-1157-2005, 2005.

Parrish, D. F., and Derber, J. C.: The National Meteorological Center's Spectral Statistical-Interpolation Analysis System, Monthly Weather Review, 120, 1747-1763, 10.1175/1520-0493(1992)120<1747:TNMCSS>2.0.CO;2, 1992.

Peng, Z., Liu, Z., Chen, D., and Ban, J.: Improving PM$_{2.5}$ forecast over China by the joint adjustment of initial conditions and source emissions with an ensemble Kalman filter, Atmospheric Chemistry and Physics, 17, 4837-4855, 10.5194/acp-17-4837-2017, 2017.

Peng, Z., Lei, L., Liu, Z., Sun, J., Ding, A., Ban, J., Chen, D., Kou, X., and Chu, K.: The impact of multi-species surface chemical observation assimilation on air quality forecasts in China, Atmospheric Chemistry and Physics, 18, 17387-17404, 10.5194/acp-18-17387-2018, 2018.

Saikawa, E., Kim, H., Zhong, M., Avramov, A., Zhao, Y., Janssens-Maenhout, G., Kurokawa, J. I., Klimont, Z., Wagner, F., Naik, V., Horowitz, L. W., and Zhang, Q.: Comparison of emissions inventories of anthropogenic air pollutants and greenhouse gases in China, Atmos. Chem. Phys., 17, 6393-6421, 10.5194/acp-17-6393-2017, 2017.

Sha, T., Ma, X., Jia, H., Tian, R., Chang, Y., Cao, F., and Zhang, Y.: Aerosol chemical component: Simulations with WRF-Chem and comparison with observations in Nanjing, Atmospheric Environment, 218, 10.1016/j.atmosenv.2019.116982, 2019.

Stavrakou, T., and Atmospheres, J. F. M. J. J. o. G. R.: Grid-based versus big region approach for inverting CO emissions using Measurement of Pollution in the Troposphere (MOPITT) data, 111, 2006.

Tang, X., Zhu, J., Wang, Z. F., Wang, M., Gbaguidi, A., Li, J., Shao, M., Tang, G. Q., and Ji, D. S.: Inversion of CO emissions over Beijing and its surrounding areas with ensemble Kalman filter, Atmospheric Environment, 81, 676-686, 10.1016/j.atmosenv.2013.08.051, 2013.

Tang, X., Zhu, J., Wang, Z., Gbaguidi, A., Lin, C., Xin, J., Song, T., and Hu, B.: Limitations of ozone data assimilation with adjustment of NO$_x$ emissions: mixed effects on NO2 forecasts over Beijing and surrounding areas, Atmospheric Chemistry and Physics, 16, 6395-6405, 10.5194/acp-16-6395-2016, 2016.

Tian, H., Liu, Y., Li, Y., Wu, C. H., Chen, B., Kraemer, M. U. G., Li, B., Cai, J., Xu, B., Yang, Q., Wang, B., Yang, P., Cui, Y., Song, Y., Zheng, P., Wang, Q., Bjornstad, O. N., Yang, R., Grenfell, B. T., Pybus, O. G., and Dye, C.: An investigation of transmission control measures during the first 50 days of the COVID-19 epidemic in China, Science, 368, 638-642, 10.1126/science.abb6105, 2020.

Wang, D., You, W., Zang, Z., Pan, X., Hu, Y., and Liang, Y.: A three-dimensional variational data assimilation system for aerosol optical properties based on WRF-Chem: design, development, and application of assimilating Himawari-8 aerosol observations, Geosci. Model Dev. Discuss., 2021, 1-54, 10.5194/gmd-2021-215, 2021.

Wang, J., Xu, X., Henze, D. K., Zeng, J., Ji, Q., Tsay, S.-C., and Huang, J.: Top-down estimate of dust emissions through integration of MODIS and MISR aerosol retrievals with the GEOS-Chem adjoint model, Geophysical Research Letters, 39,

560   n/a-n/a, 10.1029/2012gl051136, 2012.

Wang, P., Chen, K., Zhu, S., Wang, P., and Zhang, H.: Severe air pollution events not avoided by reduced anthropogenic activities during COVID-19 outbreak, Resour Conserv Recycl, 158, 104814, 10.1016/j.resconrec.2020.104814, 2020.

Wang, Y., Zhuang, G., Xu, C., and An, Z. J. A. E.: The air pollution caused by the burning of fireworks during the lantern festival in Beijing, 41, 417-431, 2007.

565   Wesely, M. L.: Parameterization of surface resistances to gaseous dry deposition in regional-scale numerical models, Atmospheric Environment (1967), 23, 1293-1304, https://doi.org/10.1016/0004-6981(89)90153-4, 1989.

Yumimoto, K., and Uno, I.: Adjoint inverse modeling of CO emissions over Eastern Asia using four-dimensional variational data assimilation, Atmospheric Environment, 40, 6836-6845, https://doi.org/10.1016/j.atmosenv.2006.05.042, 2006.

Yumimoto, K., Uno, I., Sugimoto, N., Shimizu, A., and Satake, S.: Adjoint inverse modeling of dust emission and transport
570   over East Asia, Geophysical Research Letters, 34, 10.1029/2006gl028551, 2007.

Yumimoto, K., Uno, I., Sugimoto, N., Shimizu, A., Liu, Z., and Winker, D. M.: Adjoint inversion modeling of Asian dust emission using lidar observations, Atmos. Chem. Phys., 8, 2869-2884, 10.5194/acp-8-2869-2008, 2008.

Zang, Z., Hao, Z., Pan, X., Li, Z., Chen, D., Zhang, L., and Li, Q.: Background error statistics for aerosol variables from WRF/Chem predictions in Southern California, Asia-Pacific Journal of Atmospheric Sciences, 51, 123-135, 10.1007/s13143-
575   015-0063-8, 2015.

Zang, Z., Li, Z., Pan, X., Hao, Z., and You, W.: Aerosol data assimilation and forecasting experiments using aircraft and surface observations during CalNex, Tellus B: Chemical and Physical Meteorology, 68, 10.3402/tellusb.v68.29812, 2016.

Zaveri, R. A., and Peters, L. K.: A new lumped structure photochemical mechanism for large-scale applications, Journal of Geophysical Research: Atmospheres, 104, 30387-30415, 10.1029/1999jd900876, 1999.

580   Zaveri, R. A., Easter, R. C., Fast, J. D., and Peters, L. K.: Model for Simulating Aerosol Interactions and Chemistry (MOSAIC), Journal of Geophysical Research, 113, 10.1029/2007jd008782, 2008.

Zhan, C. and Xie, M.: Land use and anthropogenic heat modulate ozone by meteorology: a perspective from the Yangtze River Delta region, Atmos. Chem. Phys., 22, 1351–1371, https://doi.org/10.5194/acp-22-1351-2022, 2022.

Zeng, Q., and Wu, L.: Optimal reduction of anthropogenic emissions for air pollution control and the retrieval of emission
585   source from observed pollutants I. Application of incomplete adjoint operator, Science China Earth Sciences, 61, 951-956, 10.1007/s11430-017-9199-2, 2018.

Zeng, Q., Wu, L., and Fei, K.: Optimal reduction of anthropogenic emissions for air pollution control and the retrieval of emission source from observed pollutants II: Iterative optimization using a positive-negative discriminant, Science China Earth Sciences, 63, 726-730, 10.1007/s11430-018-9568-5, 2020.

590   Zeng, Q., and Wu, L.: Optimal reduction of anthropogenic emissions for air pollution control and the retrieval of emission source from observed pollutants III: Emission source inversion using a double correction iterative method, Science China Earth Sciences, 10.1007/s11430-020-9860-7, 2021.

Zhang, R., Zhang, Y., Lin, H., Feng, X., Fu, T.-M., and Wang, Y.: NOx Emission Reduction and Recovery during COVID-19

in East China, Atmosphere, 11, 10.3390/atmos11040433, 2020.

595   Zheng, B., Tong, D., Li, M., Liu, F., Hong, C., Geng, G., Li, H., Li, X., Peng, L., Qi, J., Yan, L., Zhang, Y., Zhao, H., Zheng, Y., He, K., and Zhang, Q.: Trends in China's anthropogenic emissions since 2010 as the consequence of clean air actions, Atmospheric Chemistry and Physics, 18, 14095-14111, 10.5194/acp-18-14095-2018, 2018.

Zheng, B., Zhang, Q., Geng, G., Shi, Q., Lei, Y., and He, H.: Changes in China's anthropogenic emissions during the COVID-19 pandemic, Earth System Science Data Discussions, 10.5194/essd-2020-355, 2020.

600